The Astrophysical Journal, 988:253 (16pp), 2025 August 1 https://doi.org/10.3847/1538-4357/adeb7b


# Polytropic Analysis of Large-scale Compressive Fluctuations in the Solar Wind: Fluid and Kinetic Behavior

C. Ioannou[1], G. Nicolaou[1], C. J. Owen[1], D. Verscharen[1], J. T. Coburn[1], and L. Franci[2,3,4]
[1] Mullard Space Science Laboratory, University College London, Holmbury House, Dorking, RH5 6NT, UK; charalambos.ioannou.22@ucl.ac.uk
[2] Department of Mathematics, Physics and Electrical Engineering, Northumbria University, UK
[3] INAF—Institute for Space Astrophysics and Planetology, Rome, Italy
[4] Department of Physics, Imperial College London, London, UK
*Received 2025 April 10; revised 2025 June 27; accepted 2025 June 30; published 2025 July 29*

## Abstract

Large-scale compressive plasma fluctuations in the solar wind are typically characterized by an anticorrelation between the plasma density and the magnitude of the magnetic field, and thus share polarization properties with slow waves. The nature of the slow modes in the solar wind with respect to the polarization properties of the plasma has been found to be in better agreement with the magnetohydrodynamic (MHD) slow mode predictions compared to that of the kinetic slow mode. The polytropic behavior of the plasma in compressive fluctuations may provide further insight into the nature of the slow mode, since the MHD, Chew–Goldberger–Low (CGL), and kinetic slow modes predict different proton polytropic indices ($\gamma$). Using Solar Orbiter observations, we identify two 1–2 hr intervals of compressive fluctuations with a low probability of streamline crossings, determine the effective polytropic index of protons and electrons for both events, and compare them with the theoretical expectations of MHD, CGL, and kinetic slow modes. One interval exhibits characteristics of the MHD slow mode having a clear isotropic closure for the protons with $\gamma_p \approx 1.7$, while the other interval is more consistent with the kinetic slow mode. The calculated electron polytropic index is $\gamma_e \approx 0.7$ for both events. We decompose the signals into three different frequency bands and repeat our analysis, finding a similar difference in the proton polytropic behavior between the two events. A scale dependence is also observed, suggesting that kinetic effects become more prominent at smaller scales.

*Unified Astronomy Thesaurus concepts:* Solar wind (1534); Magnetohydrodynamics (1964); Space plasmas (1544); Plasma physics (2089)

## 1. Introduction

Compressive fluctuations constitute a minor component compared to the Alfvénic fluctuations in solar wind turbulence. (C. H. K. Chen 2016; J. Šafránková et al. 2019). These fluctuations are present in a wide range of scales in the solar wind, ranging from large structures in the inertial range (L. F. Burlaga & K. W. Ogilvie 1970; C. Y. Tu & E. Marsch 1995; G. G. Howes et al. 2012; C. H. K. Chen 2016; D. Verscharen et al. 2017) to kinetic scales (P. J. Kellogg & T. S. Horbury 2005; S. Yao et al. 2011). In addition to their role in the turbulent energy cascade, they also perturb the pressure and internal energy of the plasma, and thus influence the evolution of the solar wind's bulk properties (i.e., density, temperature) and can subject the plasma to various large-scale temperature anisotropy and beam instabilities (D. Verscharen et al. 2016; X. Zhu et al. 2023). Thus, investigating the nature of compressive fluctuations provides insight into how energy cascades in the solar wind, the stability of the plasma, and the plasma's internal energy as it expands in interplanetary space.

In the magnetohydrodynamic (MHD) approximation, two compressional linear modes characterizing compressive fluctuations with modulation in the magnetic field are supported for a collisional plasma, namely the fast and slow magnetosonic waves. Both waves exhibit fluctuations in the density, $\delta n$, and the magnetic field strength, $\delta|\boldsymbol{B}|$, but differ in their polarization properties. The density and the magnetic field are positively correlated for the fast mode but anticorrelated for the slow mode. In situ observations of the solar wind show that compressive fluctuations typically exhibit anticorrelation between $\delta n$ and $\delta|\boldsymbol{B}|$ (B. Bavassano & R. Bruno 1989; P. J. Kellogg & T. S. Horbury 2005; G. G. Howes et al. 2012; K. G. Klein et al. 2012; S. Yao et al. 2013; D. Verscharen et al. 2017), and thus share this polarization property with slow waves. However, the expectation for a collisionless plasma would be that MHD does not work, and thus, since the solar wind is mostly collisionless, a kinetic description of compressive fluctuations would be required.

In kinetic theory, the counterparts to the MHD slow mode, known as the kinetic slow modes (D. Verscharen et al. 2017), are the ion-acoustic (IA) wave and the nonpropagating (NP) mode, depending on the plasma's parameters (G. G. Howes et al. 2006). Observations of the polarization properties of compressive fluctuations in the solar wind were found to be in better agreement with the MHD slow-mode predictions rather than the kinetic, suggesting that the plasma behaves more fluid-like than expected. This is corroborated by measurements of the effective mean free path of the solar wind protons at 1 au, which have been shown to be three orders of magnitude smaller than the collisional mean free path (J. T. Coburn et al. 2022) and simulations of high $\beta$ collisionless plasma compressive fluctuations exhibiting fluid-like turbulent properties (R. Meyrand et al. 2019; M. W. Kunz et al. 2020).

This paper aims to discuss the polytropic behavior of compressive fluctuations in the solar wind in reference to the MHD slow mode, the Chew–Goldberger–Low (CGL) slow

mode, and the IA wave, as well as investigate the differences in the plasma's properties between the different modes using observations. A polytropic description provides closure to the plasma moments where the value of the polytropic index, $\gamma$, is a useful tool in characterizing plasma fluctuations and thermodynamic properties (see Section 2.1). Numerous studies have investigated the value of the polytropic index in the solar wind, both in the inner and outer heliosphere (T. L. Totten et al. 1995; B. Bavassano et al. 1996; J. A. Newbury et al. 1997; M. Kartalev et al. 2006; G. Nicolaou et al. 2014, 2020, 2023).

We identify two case studies of compressive fluctuations using the polarization property between $\delta n$ and $\delta|\boldsymbol{B}|$ of the slow mode, determine the polytropic index of electrons and protons, and compare them with the MHD, CGL, and IA wave predictions. Furthermore, we decompose the signal at various frequency bands and investigate how our results depend on scale. Section 2 introduces the polytropic relationship and the meaning of the effective polytropic index, illustrates the dispersion relationships of the MHD slow mode, CGL slow mode, and IA wave, and discusses the predictions of the polytropic behavior of protons and electrons for these modes. Section 3 explains how we identified the case studies, determined the effective polytropic index of protons and electrons, and carried out the multiscale analysis. Section 4 introduces the two case studies and displays our findings. In Section 5, we discuss our results and Section 6 summarizes our conclusions.

## 2. Polytropic Behavior in Compressive Waves

### 2.1. The Polytropic Equation

A polytropic process characterizes a thermodynamic transition where the ratio of energy transferred into the system as heat and as work remains constant (S. Chandrasekhar 1957). For a fluid obeying the ideal gas law, with density, $n$, and isotropic pressure, $P$, (or temperature, $T$), this is expressed as

$$P \propto n^{\gamma} \quad \text{or} \quad T \propto n^{\gamma-1}, \tag{1}$$

where $\gamma$ is the polytropic index. The value of $\gamma$ provides insight into a fluid's heat dynamics and effective kinetic degrees of freedom, $f$, as it undergoes a thermodynamic transition (G. Livadiotis & G. Nicolaou 2021). For the special case where there is zero heat transfer during the process, known as an adiabatic process, the polytropic index can be expressed in terms of $f$ by

$$\gamma = 1 + 2/f. \tag{2}$$

Thus, for a plasma with $f = 1$, an adiabatic process has a polytropic index of $\gamma = 3$; while for $f = 3$, the index will be $\gamma = 5/3$. A process at a constant temperature, known as an isothermal process, is characterized by $\gamma = 1$, a process at a constant pressure, known as isobaric, is characterized by $\gamma = 0$, and a process at a constant volume, known as isochoric, is characterized by $\gamma = \infty$.

In magnetized plasmas, the distributions are often anisotropic and thus require two pressures (temperatures) to describe the plasma, one parallel and one perpendicular to $\boldsymbol{B}$. Under this consideration, it is useful to introduce the parallel, $\gamma_{\parallel}$, and perpendicular, $\gamma_{\perp}$, polytropic indices which characterize the relationship between $n$ and the parallel, $P_{\parallel}$, and perpendicular, $P_{\perp}$, pressure (or parallel, $T_{\parallel}$, and perpendicular, $T_{\perp}$, temperature) by

$$P_{\parallel} \propto n^{\gamma_{\parallel}} \quad \text{or} \quad T_{\parallel} \propto n^{\gamma_{\parallel}-1}, \tag{3}$$

and

$$P_{\perp} \propto n^{\gamma_{\perp}} \quad \text{or} \quad T_{\perp} \propto n^{\gamma_{\perp}-1}. \tag{4}$$

### 2.2. Fluid and Kinetic Slow Modes

In the MHD limit, the linear dispersion relation of the slow mode is given by

$$\omega^{\mathrm{MHD}} = \pm k C_{-}, \tag{5}$$

where

$$C = V_{\mathrm{A}}\left[\frac{1}{2}\left(1 + \frac{\gamma}{2}\beta_p\right) - \frac{1}{2}\sqrt{\left(1 + \frac{\gamma}{2}\beta_p\right)^2 - 2\gamma\beta_p\cos^2\theta}\right]^{\frac{1}{2}}, \tag{6}$$

$V_{\mathrm{A}} = |\boldsymbol{B}|/\sqrt{4\pi n_p m_p}$ is the MHD Alfvén speed, $m_p$ is the proton mass, $\beta_p = 8\pi n_p k_{\mathrm{B}} T_p/\boldsymbol{B}^2$, $k_{\mathrm{B}}$ is the Boltzmann constant, and $\theta$ is the angle between the wavevector, $\boldsymbol{k}$, and $\boldsymbol{B}$. As per the typical assumptions of ideal and isotropic MHD, the pressure (and temperature) is isotropic and is related to the density via a polytropic closure. Thus, plasma experiencing compressive fluctuations characterized by the MHD slow mode exhibits a polytropic closure between the density and the isotropic pressure. Regarding the value of the polytropic index, while $\gamma$ appears as a free parameter in the dispersion relation, we can form predictions based on the ambient solar wind conditions. We expect protons to exhibit adiabatic behavior with $\gamma_p = 5/3$ (E. Marsch & A. K. Richter 1984; G. Nicolaou & G. Livadiotis 2019; G. Nicolaou et al. 2023) and electrons to behave isothermally with $\gamma_e \approx 1$ due to their large heat flux (J. B. Abraham et al. 2022).

In the case of the kinetic slow mode, assuming a bi-Maxwellian background distribution function, the least damped propagating mode with slow-mode poralization is an IA wave with a linear dispersion relation in the gyrokinetic limit of

$$\omega_r^{IA} = \pm|k|c_s, \tag{7}$$

where (S. P. Gary 1993; Y. Narita & E. Marsch 2015)

$$c_s = \sqrt{\frac{3k_{\mathrm{B}}T_{\parallel,p} + k_{\mathrm{B}}T_{\parallel,e}}{m_p}} \tag{8}$$

is the IA speed. Comparing this dispersion relation with that of two-fluid theory allows us to form expectations regarding the polytropic behavior of the protons and electrons during an IA wave (S. P. Gary 1993). In two-fluid theory, the dispersion relation is given by

$$\omega_r^{F} = \pm|k|c_F, \tag{9}$$

where

$$c_F = \sqrt{\frac{\gamma_p^F k_{\mathrm{B}}T_{\parallel,p} + \gamma_e^F k_{\mathrm{B}}T_{\parallel,e}}{m_p}} \tag{10}$$

is the two-fluid wave speed, and $\gamma_p^F$ and $\gamma_e^F$ are the proton and electron two-fluid polytropic indices, respectively. Assuming a polytropic closure and directly comparing (8) and (10) shows that $\gamma_{p\parallel} = 3$ and $\gamma_{e\parallel} = 1$ for the IA wave (S. P. Gary 1993). This suggests that protons exhibit one-dimensional adiabatic behavior due to the degree of freedom along the magnetic field direction, while electrons behave isothermally due to their large heat flux. For an IA wave, a polytropic closure is expected between $n$ and $P_\parallel$ for both protons and electrons.

Another fluid model we can consider to describe plasma dynamic fluctuations is the Chew, Goldberger, & Low model (G. F. Chew et al. 1956). In the CGL model, the slow-mode dispersion relation is (P. Hunana et al. 2019)

$$\omega_{\rm CGL}^2 = \frac{(kV_{\rm A})^2}{2}\left[1 + \alpha_p\beta_\parallel\left(1 - \frac{1}{2}\cos^2\theta\right) + \beta_\parallel\cos^2\theta\right] - A, \tag{11}$$

where

$$A = \frac{1}{2}\sqrt{\left[1 + \alpha_p\beta_\parallel\left(1 - \frac{1}{2}\cos^2\theta\right) - 2\beta_\parallel\cos^2\theta\right]^2 + \alpha_p^2\beta_\parallel^2\sin^2\theta\cos^2\theta},$$

$\alpha_p = \frac{T_\perp}{T_\parallel}$ and $\beta_\parallel$ is determined using $T_\parallel$. A polytropic closure for protons can also be incorporated in the CGL model by introducing the parallel, $\xi_\parallel$, and perpendicular, $\xi_\perp$, CGL polytropic indices defined by

$$\frac{d}{dt}\left(\frac{P_{p,\parallel}|\boldsymbol{B}|^{\xi_\parallel-1}}{n_p^{\xi_\parallel}}\right) = 0 \tag{12}$$

and

$$\frac{d}{dt}\left(\frac{P_{p,\perp}}{n_p|\boldsymbol{B}|^{\xi_\perp-1}}\right) = 0. \tag{13}$$

These polytropic indices differ from the MHD ones (represented with the letter $\gamma$). In the classical CGL case, the fluid is modeled by the double adiabatic equations and thus $\xi_\parallel = 3$ and $\xi_\perp = 2$, while for the isothermal case $\xi_\parallel = 1$ and $\xi_\perp = 1$ (B. Abraham-Shrauner 1973; L. N. Hau & B. U. O. Sonnerup 1993; P. Hunana et al. 2019).

## 3. Observational Methods

### 3.1. Data Processing and Case Study Criteria

We use observations from the Solar Wind Analyser (SWA) suite of instruments (C. J. Owen et al. 2020), the MAG magnetometer (T. S. Horbury et al. 2020) and the Radio and Plasma Waves (RPW; M. Maksimovic et al. 2020) instrument aboard Solar Orbiter (D. Müller et al. 2020). Specifically, we obtain the proton density and pressure tensor from ground moments of the velocity distribution functions (VDFs) constructed from SWA-Proton and Alpha Sensor (PAS) measurements, the electron densities from RPW, and the magnetic field data from MAG. We determine the electron density and pressure used in the polytropic analysis by calculating moments of the 2D pitch angle–energy distribution function measured by the SWA-Electron Analyser Sensor (EAS). We calculate the moments over the entire energy range of EAS after shifting the distribution by the spacecraft potential measured by RPW. This shift significantly reduces low-energy electron contamination from photoelectrons and other spacecraft potential effects (G. Nicolaou et al. 2021b; S. Štverák et al. 2025). To validate the electron moments from EAS, we cross-check the determined densities with the RPW densities. The VDFs in the instrument frames, magnetic field vectors, and PAS moments are available at the Solar Orbiter Archive.[5]

Assuming the Taylor frozen-in flow hypothesis, we use the polarization property of the slow mode as an observable marker for identifying compressive fluctuations. Intervals with a Pearson correlation coefficient between $n_p$ and $|\boldsymbol{B}|$, $R_p(n_p, |\boldsymbol{B}|)$, less than $-0.6$, and a maximum $n_p$ and $|\boldsymbol{B}|$ fluctuations from the average value greater than 10% were considered. The intervals we study are one to two hours long, long enough to sample the inertial range and allow for multiscale analysis and short enough to avoid times when the spacecraft samples different streams.

Streamline crossings invalidate the application of the polytropic relation Equation (1) (T. L. Totten et al. 1995; J. A. Newbury et al. 1997; M. Kartalev et al. 2006; G. Nicolaou et al. 2014; G. Nicolaou & G. Livadiotis 2017). Thus, to accurately determine $\gamma$, one should ensure that the interval analyzed contains plasma from the same solar wind structure. The variability of the Bernoulli integral (BI), which describes the energy conservation in a fluid, is an indicator of potential streamline crossings (M. Kartalev et al. 2006). At 1 au, the dynamic term, $\mathrm{BI}_D = V_{p,b}^2/2$, of BI dominates over the thermal and magnetic terms, as demonstrated by G. Nicolaou et al. (2021a). To ensure that this condition also holds for both intervals in this study, we determine the proton thermal and magnetic terms of BI. We find that $\mathrm{BI}_D$ is at least an order of magnitude greater than the sum of the thermal and magnetic terms throughout both intervals. Thus, we use $\mathrm{BI}_D$ as a proxy for BI. We define the variability of BI, $\Delta$BI, as

$$\Delta\mathrm{BI} = \frac{\sigma_{\mathrm{BI}_D}}{\langle \mathrm{BI}_D\rangle}, \tag{14}$$

where $\sigma_{\mathrm{BI}_D}$ and $\langle \mathrm{BI}_D\rangle$ are the standard deviation and mean of $\mathrm{BI}_D$ across the entire interval, respectively. Only intervals with $\Delta\mathrm{BI} < 0.025$ are considered; a similar condition used by C. Katsavrias et al. (2024). This condition increases the probability that the analyzed interval corresponds to an individual streamline, but does not guarantee it.

### 3.2. Polytropic and Multiscale Analysis

Taking the log of Equation (1) yields

$$\log P = \gamma\,\log n + \text{const.} \tag{15}$$

We calculate $\gamma$ by applying a least square linear regression to $\log P$ versus $\log n$ data points and calculate the slope. Using $P_\parallel$, $P_\perp$, and $P$ allows for calculating the effective parallel, $\gamma_\parallel$, effective perpendicular, $\gamma_\perp$, and effective isotropic, $\gamma$, indices, respectively.

[5] https://soar.esac.esa.int/soar/

Similarly, using the conservation form of Equations (12) and (13) and taking the logarithm, we find

$$\log \frac{P_{\parallel}}{n} = (\xi_{\parallel} - 1) \log \frac{n}{|\boldsymbol{B}|} + \text{const}, \tag{16}$$

and

$$\log \frac{P_{\perp}}{n} = (\xi_{\perp} - 1) \log|\boldsymbol{B}| + \text{const}. \tag{17}$$

We calculate $\xi_{\parallel}$ by applying a least squares linear regression to a $\log P_{\parallel}/n$ versus $\log n/|\boldsymbol{B}|$ plot and calculate the slope. Similarly, we calculate $\xi_{\perp}$ by applying a least squares linear regression to a $\log P_{\perp}/n$ versus $\log|\boldsymbol{B}|$ plot.

We decompose the density, pressure, and magnetic field signals using the Multivariate Fast Iterative Filtering (MvFIF) algorithm (A. Cicone & E. Pellegrino 2022) to perform our analysis across multiple scales. Unlike wavelet-based techniques, MvFIF performs the time-frequency analysis of multivariate signals without requiring a preselected base signal or making any a priori assumptions on the signal (A. Cicone & E. Pellegrino 2022). We then perform polytropic analysis on the decomposed density and pressure within frequency bands, using the same procedure as before, to determine $\gamma$ at different scales. To examine the slow-mode polarization condition throughout the interval at different scales, we determine the cross-wavelength coherence between $n_p$ and $|\boldsymbol{B}|$. We calculate this using the PIWavelet[6] Python package, which is a Python interface for the Matlab package for wavelet, cross-wavelet, and coherence-wavelet analysis (A. Grinsted et al. 2004).

## 4. Results

We report two case studies of compressive fluctuations observed by the Solar Orbiter spacecraft. The first interval, referred to as CS1, was observed on 2021 July 28 from 07:40 to 08:40 UT and the second, referred to as CS2, was observed on 2021 August 5 from 00:30 to 02:00 UT. The subscripts "1" and "2" designate quantities for intervals CS1 and CS2, respectively. Figures 1(a)–(f) and 2(a)–(f) show the time series of plasma and field parameters for CS1 and CS2, respectively, and Table 1 summarizes the average properties of both events. Panel (a) shows the electron and proton density, panel (b) shows $\boldsymbol{B}$ in the RTN frame, panel (c) shows the normalized fluctuations from the mean, $\delta x/x_0$, where $x_0 = \sum_{i=1}^{N} x_i/N$, $N$ is the total number of data points in the interval and $\delta x = x - x_0$, for $n_e$, $n_p$ and $|\boldsymbol{B}|$, panel (d) shows the radial proton bulk speed, panel (e) shows the electron and proton temperature, and panel (f) shows $T_{p\perp}/T_{p\parallel}$.

### 4.1. Polytropic Index

The proton and electron density time series share almost identical profiles in both events, except that $n_e$ is marginally larger (≈6%) than $n_p$. This difference in particle density is, however, expected due to the presence of alpha and higher-charged ions, requiring $n_p < n_e$ to achieve quasi-neutrality. The density difference appears stronger in CS2, especially in the first half of the event, which is possibly due to a larger $\alpha$-particle composition of the plasma when compared to CS1, although alpha densities are not available to check this assumption. Both events have a similar magnetic field strength of just over 5 nT. In CS1, the field is mainly in the $B_N$ direction, with a weak $B_R$ component. In contrast, in CS2, the field's direction varies throughout the event. While $B_R$ experiences minor fluctuations around −5 nT, there are multiple sharp variations and reversals of $B_N$ and $B_T$. The normalized fluctuations in the magnetic field are anticorrelated with the density fluctuations, for both events, as is evident in Figures 1(c) and 2(c), which is consistent with the expectations of the slow mode. CS1 exhibits a stronger anticorrelation, with a Pearson correlation coefficient of −0.905, compared to −0.677 for CS2.

To further examine the correlation between density and the magnetic field, we calculate the squared cross-wavelet coherence (C. Torrence & G. P. Compo 1998), using the Morlet wavelet, for both events, shown in Figures 3 and 4. The white dashed line shows the cone of influence (COI), indicating the regions where the cross-wavelet coherence is potentially affected by edge-effect artefacts. The COI in CS2 is not symmetric due to data gaps in the period before the event. As expected, both events exhibit strong coherence between $n$ and $|\boldsymbol{B}|$. Despite this, CS2 contains short intervals with little correlation between the two parameters, in contrast to CS1, where the coherence is clear throughout the event, in line with the correlation coefficients calculated for both events. However, there is a clear exception at high frequencies, where the coherence is not evident in either event.

Both events occur in slow solar wind conditions with similar average bulk properties. The plasma is colder in CS1, and the protons are colder than the electrons in both events. Both events also have a comparable $\beta_{p,\parallel}$, which is just above unity. $\Delta\text{BI} < 0.025$ for both events, which suggests a low probability of streamline crossings.

Figures 5 and 6 show plots of electron and proton pressure versus density, including the polytropic index fits for CS1 and CS2, respectively. The color of the data points represents the time instance of the corresponding measurement in the interval. We perform linear regression between the pressure and density data, indicated by the black line, to determine $\gamma$. The error represents only the statistical error of the fit based on a least squares calculation. Additionally, we calculate the Pearson correlation coefficient, $R_p$, between the logarithmic pressure and density. Panels (a)–(c) show the protons results, while Panels (d)–(f) show the electron results. Panels (a) and (d) show the results using $P_{\parallel}$, panels (b) and (e) using $P_{\perp}$ and panels (c) and (f) using $P$. The range of the $n$ and $P$ axes is the same for all plots to visualize the gradients of the linear fits more clearly.

In CS1, we observe a large correlation coefficient between $P_p$ and $n_p$ in all cases, with $R_p > 0.9$, suggesting a proton polytropic closure. In the isotropic case, the linear fit determines $\gamma_{1,p} \approx 1.7$, which is close to the adiabatic value for a system with $f = 3$. The value of the indices in the parallel and perpendicular directions diverge slightly from the adiabatic value, where $\gamma_{1,p,\parallel} \approx 1.9$ is larger while $\gamma_{1,p,\perp} \approx 1.6$ is smaller than $\gamma_{1,p}$. Electrons exhibit subisothermal behavior ($\gamma < 1$) in all cases. The correlation coefficient is large for all electron cases with $R_p > 0.9$, suggesting a polytropic closure is valid for electrons.

Electrons in CS2 are described by a subisothermal polytropic index in all cases, with similar $R_p$ values as in CS1, suggesting that an electron polytropic closure is also

[6] https://github.com/duducosmos/PIWavelet

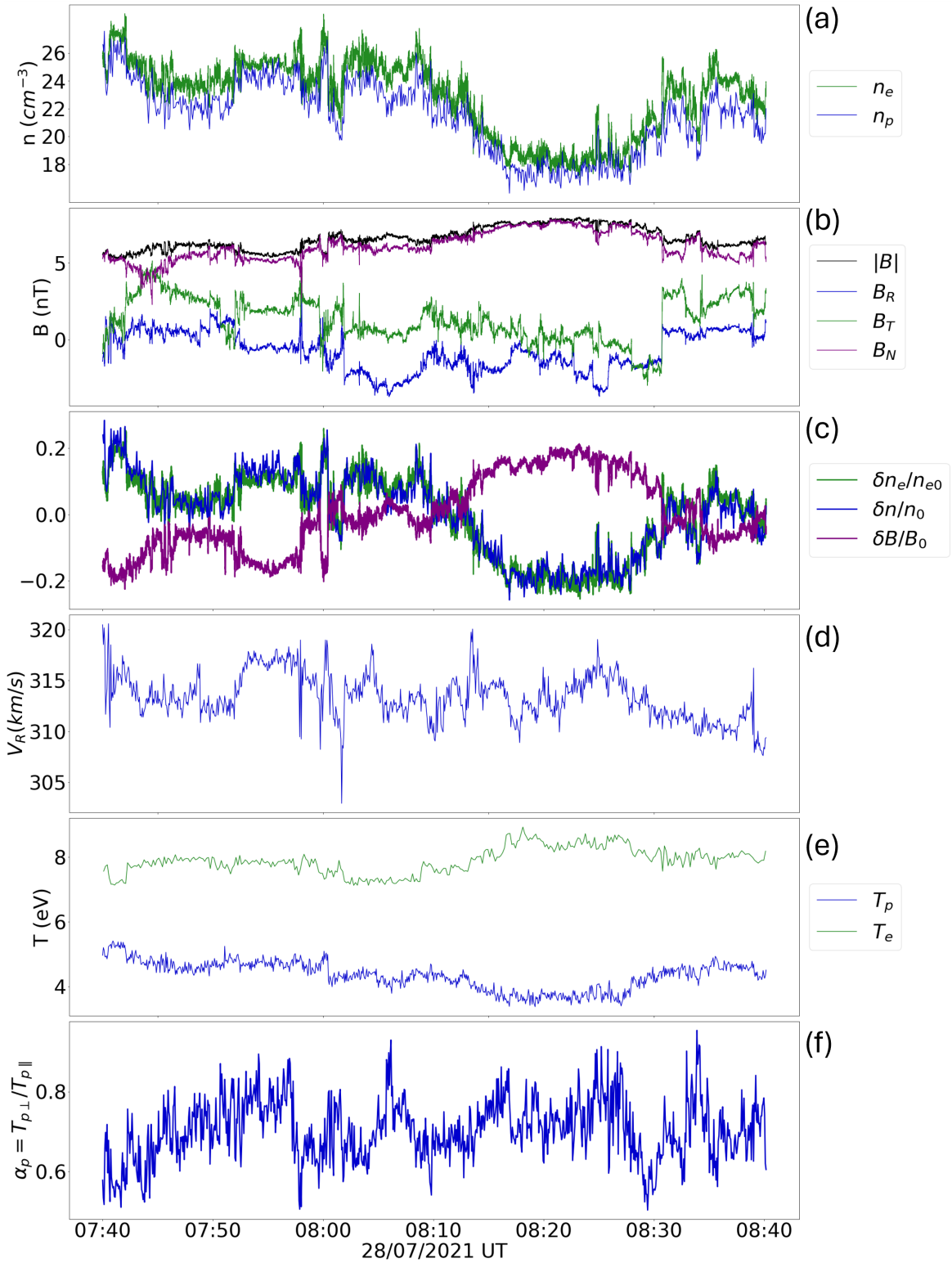


**Figure 1.** Time series for event CS1: (a) proton, $n_p$, and electron, $n_e$, density, (b) magnetic field, $\boldsymbol{B}$, in RTN frame, (c) $n_p$, $n_e$ and $|\boldsymbol{B}|$ normalized fluctuations, (d) radial proton bulk speed, $V_R$, (e) proton, $T_p$, and electron, $T_e$, temperature, and (f) proton temperature anisotropy, $\alpha_p = T_{p\perp}/T_{p\parallel}$.

applicable in CS2. The protons, however, exhibit different behavior between the two events. A large correlation coefficient is again observed in the parallel case with $R_p = 0.783$, suggesting a polytropic closure with $P_{p,\parallel}$, but the closure is not clear in the perpendicular component as $R_p = 0.491$. The values of the parallel and perpendicular indices diverge significantly, since $\gamma_{2,p,\parallel}$ is much larger with $2.792 \pm 0.060$ while $\gamma_{2,p,\perp}$ lies in the subisothermal regime with $0.840 \pm 0.041$. From Figure 6(c), two clusters separated by time can be observed in the interval, which suggests that a polytropic closure is present in these cases if the event is further segregated.

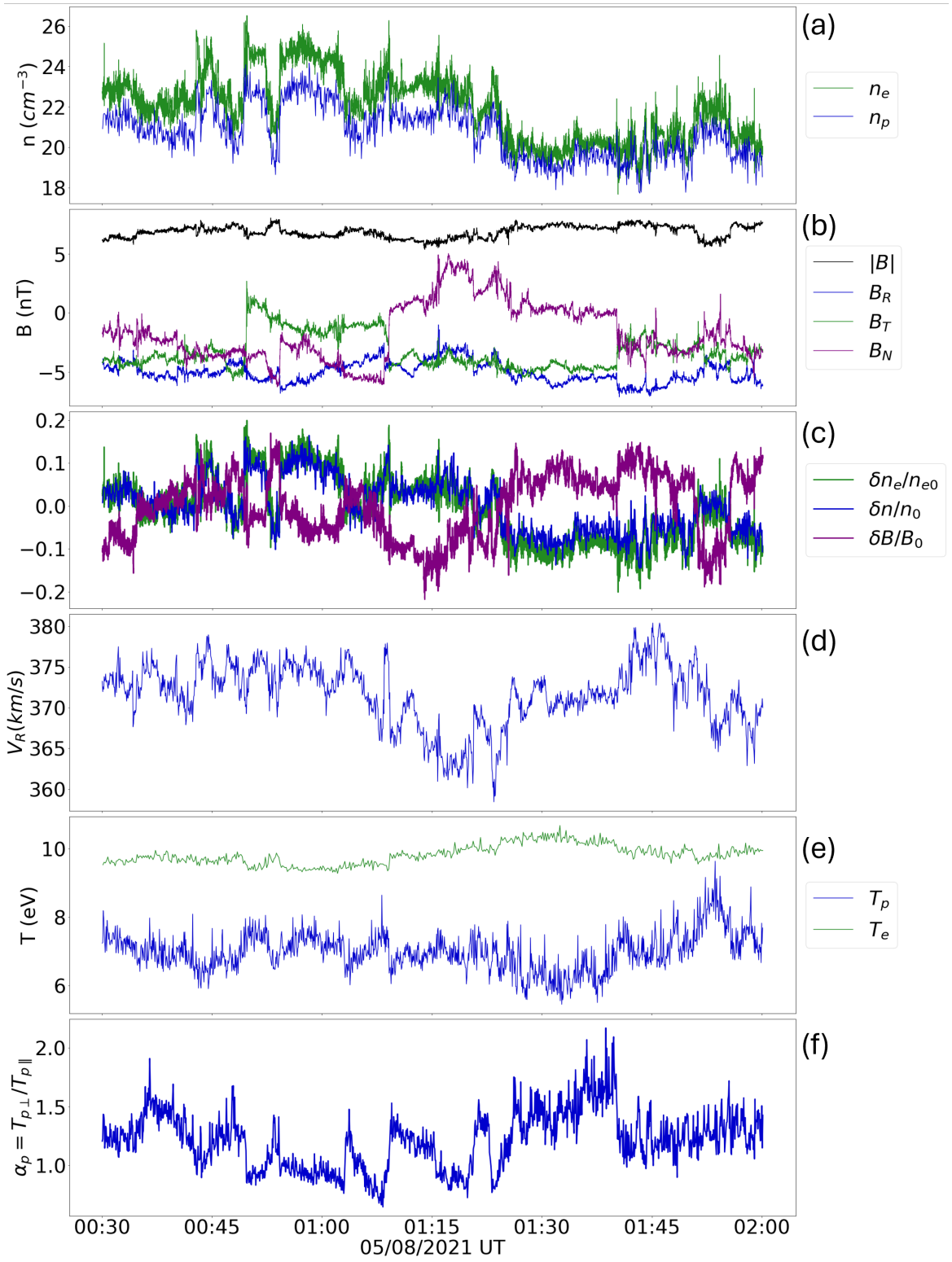


**Figure 2.** Time series for event CS2: (a)–(f) same as in Figure 1.

### *4.2. Multiscale Analysis*

We decomposed the $P$, $n$, and $|\boldsymbol{B}|$ signals at various frequencies using the MvFIF algorithm, allowing us to perform the same analysis as before, only on signals within a particular frequency band. Three distinct frequency bands are selected for each event, separated by the black lines in Figures 3 and 4. We refer to them as high frequency (HF), intermediate frequency (IF), and low frequency (LF). The frequency range of each band is shown in Table 2.

The MvFIF algorithm decomposes the signal into simple oscillating components of varying frequency named intrinsic mode functions (IMFs). To form the three frequency bands, we sum together the IMFs corresponding to the frequencies within

**Table 1**
Average Bulk and Plasma Parameters of Case Study 1 (CS1) and Case Study 2 (CS2)

| | Date ; Time (UT) | $R$ (au) | $\langle n_p \rangle$ ($cm^{-3}$) | $\langle T_p \rangle$ (eV) | $\langle T_e \rangle$ (eV) | $\langle V_b \rangle$ ($km\ s^{-1}$) | $\langle \beta_{p\parallel} \rangle$ | $R_p(n_p, \lvert \boldsymbol{B} \rvert)$ | $\Delta$BI |
|---|---|---|---|---|---|---|---|---|---|
| CS1 | 28/07/21; 07:40–08:40 | 0.80 | 21.5 | 4.35 | 7.89 | 314 | 1.20 | −0.905 | 0.014 |
| CS2 | 05/08/21; 00:30–02:00 | 0.75 | 20.8 | 6.99 | 9.82 | 371 | 1.15 | −0.677 | 0.021 |

**Note.** $R$ is the distance from the Sun, $\langle n_p \rangle$ is the average proton density, $\langle T_p \rangle$ and $\langle T_e \rangle$ are the average proton and electron temperatures, $\langle V_b \rangle$ is the average proton bulk speed, $\langle \beta_{p,\parallel} \rangle$ is the average parallel proton beta, $R_p(n_p, |\boldsymbol{B}|)$ is the Pearson correlation coefficient between $n_p$ and $|\boldsymbol{B}|$, and $\Delta$BI is the variability of the Bernoulli integral.

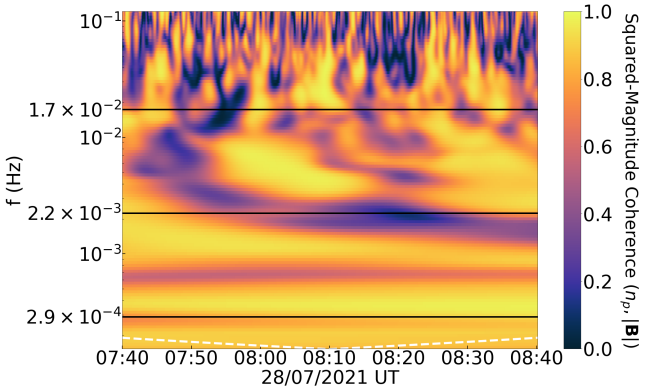


**Figure 3.** Cross-wavelength coherence between $n_p$ and $|\boldsymbol{B}|$ for CS1. The white dashed line indicates the COI. The horizontal black lines indicate the boundaries between the three different frequency bands analyzed.

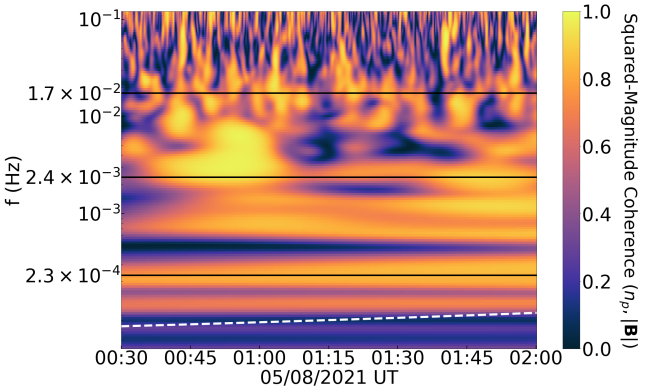


**Figure 4.** Cross-wavelength coherence between $n_p$ and $|\boldsymbol{B}|$ for CS2. Same format as Figure 3.

each band. The decomposition into the different IMFs is purely data-driven, meaning that the frequency and the shape of each IMF are not assigned a priori, but are determined empirically by the algorithm (for details, see N. E. Huang et al. 1998; A. Cicone & E. Pellegrino 2022). A detailed explanation of how the algorithm works and how it can be used to separate the different contributions to a (numerical) signal that correspond to different (spatial) frequency bands (large, intermediate, and small scales) can be found in E. Papini et al. (2020). We decompose both intervals into 50 IMFs (plus one additional component, the residual trend signal), and we set identical IMF ranges for the HF, IF, and LF bands between the two events. This is why the boundaries between the bands are not identical between CS1 and CS2. We set the IMF range for the HF band to include the noncoherent regions observed at high frequencies in Figures 3 and 4, and for the IF and LF bands to span approximately an order of magnitude in frequency. The frequency space examined by the IF and LF bands, while not identical between the two case studies, is large enough in relation to the boundary differences to allow for a comparison between the two events.

We perform identical correlation coefficient and polytropic analysis procedures as before on the signals for each frequency band. Figures 7 and 8 show the proton and electron results, respectively, for each frequency band regarding CS1 and Figures 9 and 10 show the results regarding CS2. The HF results are shown in panels (a), (d), and (g), the IF results in panels (b), (e), and (h), and the LF results in panels (c), (f), and (i). Figure 11 summarizes the multiscale polytropic index results for protons (a) and electrons (b). The Pearson correlation coefficient between $n_p$ and $|\boldsymbol{B}|$, $R_p(n_p, |\boldsymbol{B}|)$, and polytropic index results for both events are summarized in Table 2.

#### 4.2.1. High Frequency Band

The $n$ and $|\boldsymbol{B}|$ anticorrelation is weakest in the HF band, especially for CS2, which is consistent with Figures 3 and 4. In this frequency band, the electrons exhibit subisothermal behavior in both events, and the values of the polytropic indices in all three directions are comparable. The proton behavior also shows little deviation between the two events as $1 < \gamma_p^{\rm HF} < 5/3$ and $\gamma_{p,\perp}^{\rm HF} < \gamma_p^{\rm HF} < \gamma_{p,\parallel}^{\rm HF}$.

#### 4.2.2. Intermediate Frequency Band

In the IF band, protons exhibit different behavior in the two events. The polytropic closure is applicable in all IF cases in CS1 because $R_p > 0.85$. $\gamma_{1,p}^{\rm IF}$ is near the adiabatic value of 5/3, assuming $f = 3$. The parallel and perpendicular indices diverge similarly to the results of the full signal, but to a greater extent as $\gamma_{1,p,\parallel}^{\rm IF}$ increases to $2.305 \pm 0.034$, while $\gamma_{1,p,\perp}^{\rm IF}$ drops close to the isothermal index. The polytropic closure is not as clear in CS2 in the perpendicular direction as $R_p \approx 0.5$. In contrast to CS1, protons behave subisothermally in the perpendicular direction, while $\gamma_{2,p,\parallel}^{\rm IF}$ is much larger with a value of $2.840 \pm 0.073$, which is similar to that of the full signal. Regarding CS2, electrons again exhibit subisothermal behavior with $R_p > 0.9$, suggesting a polytropic closure. A closure is also observed in CS1, albeit with weaker correlation coefficients, where the indices in all three cases increase, most notably in the parallel direction where $\gamma_{1,e,\parallel}^{\rm IF}$ surpasses the isothermal threshold.

#### 4.2.3. Low Frequency Band

The proton behavior in the LF band does not vary significantly from that in the IF band. Compared to the IF

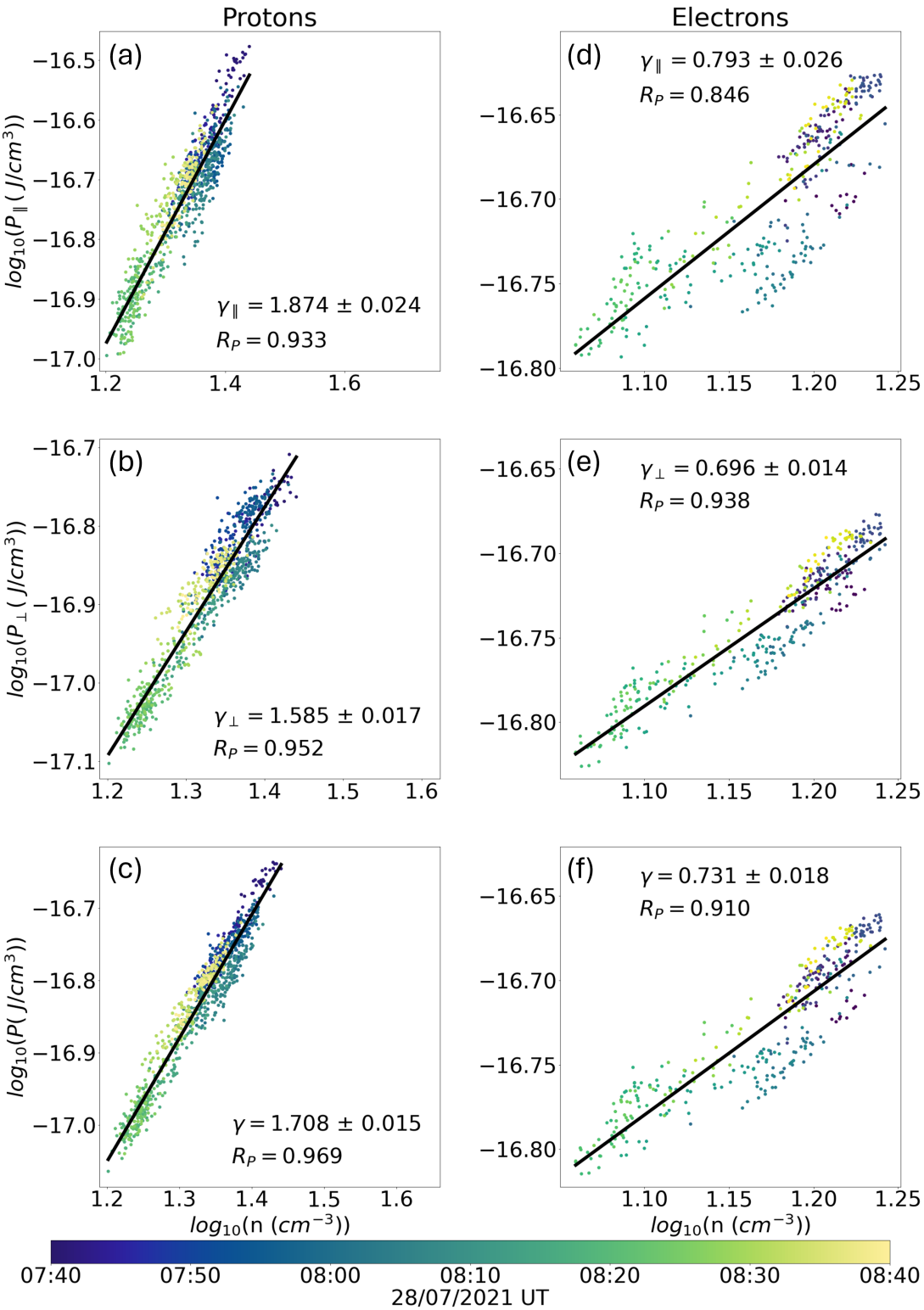


**Figure 5.** Polytropic index results for protons and electrons in CS1. $R_p$ is the Pearson correlation coefficient. Panels (a)–(c) show the proton results and panels (d)–(f) show the electron results. Panels (a) and (d) show the parallel, panels (b) and (e) the perpendicular, and panels (c) and (f) the isotropic index results. The color of the data points represents the time instance of the corresponding measurement in the interval.

results, $\gamma_{p,\parallel}$ is smaller with $\gamma^{\rm LF}_{p,\parallel} < \gamma^{\rm IF}_{p,\parallel}$, while $\gamma_{p,\perp}$ is larger with $\gamma^{\rm LF}_{p,\perp} > \gamma^{\rm IF}_{p,\perp}$ in both events. The separation between the two indices remains larger in CS2. $\gamma^{\rm LF}_p$ for both events is comparable and close to the adiabatic value for $f = 3$. Electrons again exhibit subisothermal behavior in both events.

### 4.3. CGL Results

Figures 12 and 13 show the CGL analysis results for CS1 and CS2, respectively. A CGL polytropic closure can be seen in both cases in CS1, where $\xi_{1,\parallel} = 1.487 \pm 0.012$ and $\xi_{1,\perp} = 0.244 \pm 0.014$. The polytropic closure is less evident in CS2, especially in the perpendicular case as $|R_p| < 0.25$.

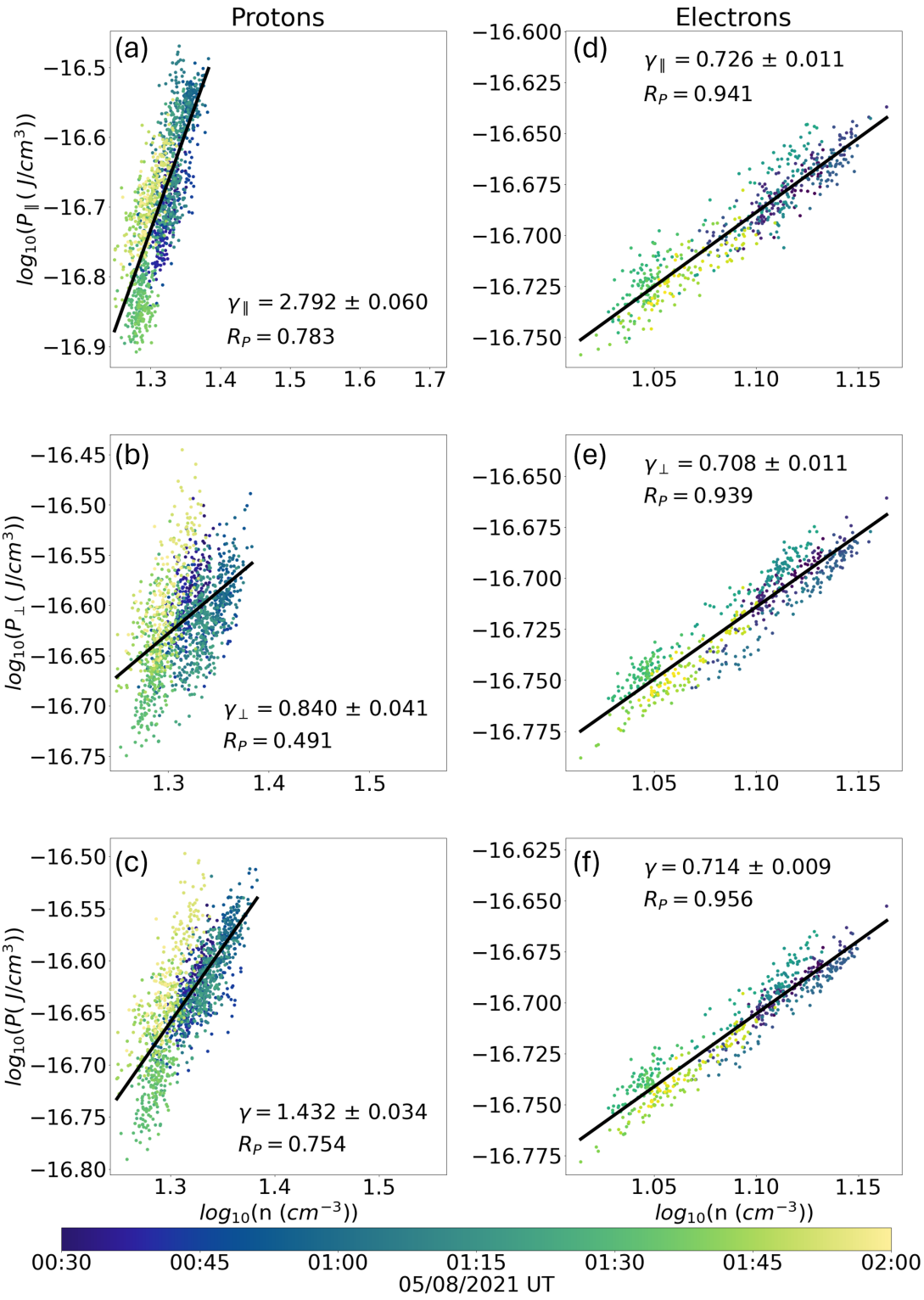


**Figure 6.** Polytropic index results for protons and electrons in CS2. Same format as in Figure 5.

For both events, $\xi_\parallel$ and $\xi_\perp$ differ from the adiabatic ($\xi_\parallel = 3$, $\xi_\perp = 2$) and isothermal ($\xi_\parallel = 1$, $\xi_\perp = 1$) values.

## 5. Discussion

### 5.1. Protons

The proton polytropic behavior in CS1 is in agreement with the MHD predictions, suggesting that there is little net heat exchange experienced by the protons. For the MHD slow mode, we assume an isotropic plasma, meaning that $\gamma_{p,\parallel}$ and $\gamma_{p,\perp}$ have identical behavior. In CS1, $\gamma_{1,p,\parallel} \neq \gamma_{1,p,\perp}$, suggesting that there exists some anisotropy in the plasma, which is also evident in the temperature profile in Figure 1(f). Despite this, the ability of the isotropic closure to describe the plasma, having a good Pearson correlation coefficient, provides compelling evidence of the fluid-like behavior of

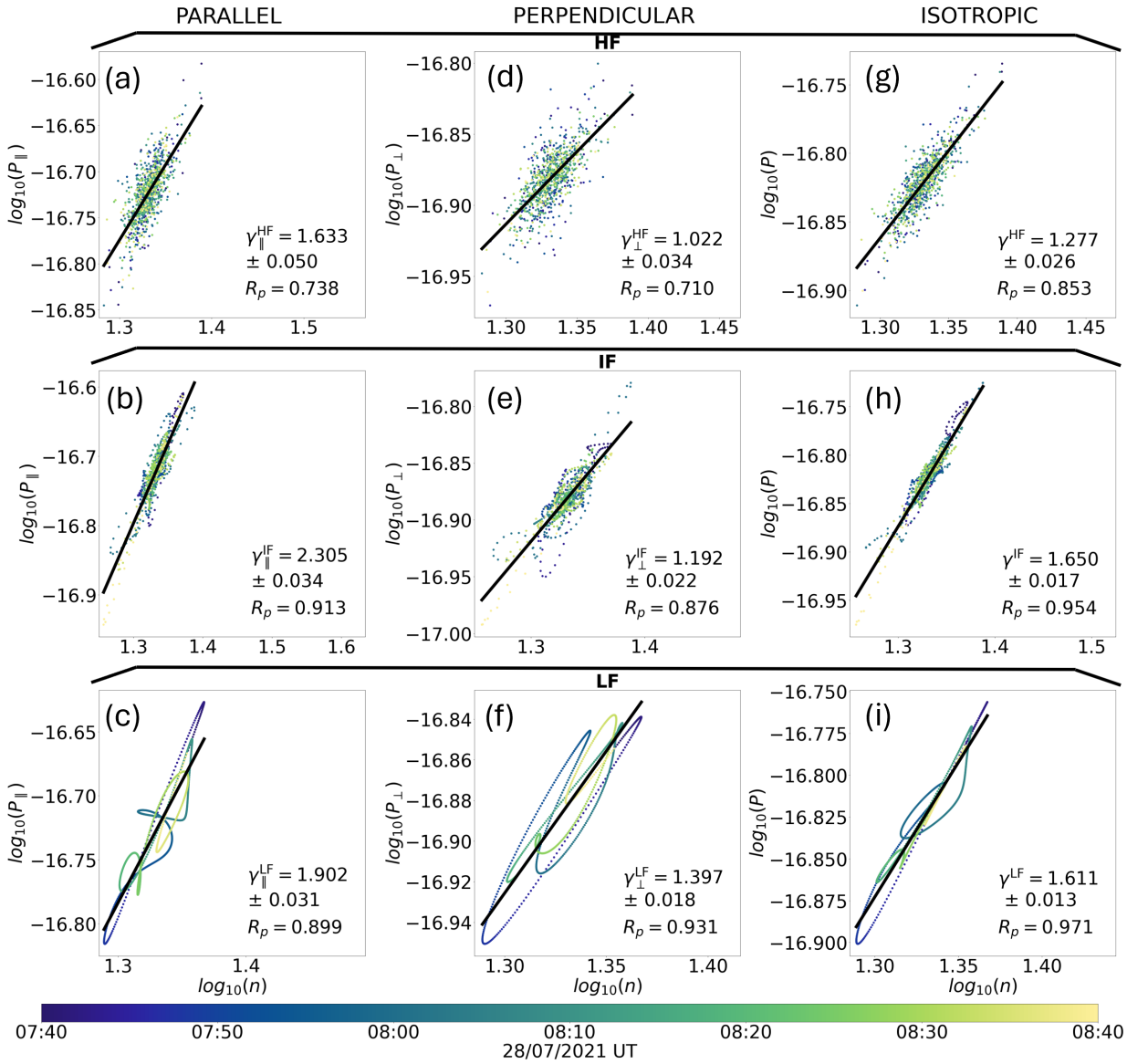


**Figure 7.** Polytropic index results of the decomposed signals for the protons in CS1. $R_p$ is the Pearson correlation coefficient. Panels (a), (d), and (g) show the HF, panels (b), (e), and (h) show the IF, and panels (c), (f), and (i) show the LF results. Panels (a)–(c) show the parallel, panels (d)–(f) the perpendicular, and panels (g)–(i) the isotropic polytropic indices.

**Table 2**
Polytropic Index Results of Decomposed Signals for the LF, IF, and HF Bands for Protons and Electrons

| | | | Frequency Range (Hz) | $R_p(n_p, \lvert\boldsymbol{B}\rvert)$ | Parallel ($\gamma_\parallel$) | Perpendicular ($\gamma_\perp$) | Isotropic ($\gamma$) |
|---|---|---|---|---|---|---|---|
| Case 1 | Protons | LF | $2.89 \times 10^{-4} - 2.24 \times 10^{-3}$ | −0.873 | 1.902 ± 0.031 | 1.397 ± 0.018 | 1.611 ± 0.013 |
| | | IF | $2.24 \times 10^{-3} - 1.74 \times 10^{-2}$ | −0.870 | 2.305 ± 0.035 | 1.192 ± 0.022 | 1.650 ± 0.017 |
| | | HF | $1.74 \times 10^{-2} - 2.50 \times 10^{-1}$ | −0.651 | 1.633 ± 0.050 | 1.022 ± 0.034 | 1.277 ± 0.026 |
| | Electrons | LF | $2.89 \times 10^{-4} - 2.24 \times 10^{-3}$ | −0.986 | 0.772 ± 0.022 | 0.678 ± 0.011 | 0.712 ± 0.014 |
| | | IF | $2.24 \times 10^{-3} - 1.74 \times 10^{-2}$ | −0.844 | 1.072 ± 0049 | 0.828 ± 0.025 | 0.915 ± 0.032 |
| | | HF | $1.74 \times 10^{-2} - 1.00 \times 10^{-1}$ | −0.735 | 0.750 ± 0.040 | 0.760 ± 0.024 | 0.756 ± 0.027 |
| Case 2 | Protons | LF | $2.32 \times 10^{-4} - 2.38 \times 10^{-3}$ | −0.813 | 2.600 ± 0.088 | 1.196 ± 0.039 | 1.618 ± 0.031 |
| | | IF | $2.38 \times 10^{-3} - 1.74 \times 10^{-2}$ | −0.764 | 2.840 ± 0.073 | 0.866 ± 0.041 | 1.449 ± 0.034 |
| | | HF | $1.75 \times 10^{-2} - 2.50 \times 10^{-1}$ | −0.501 | 1.608 ± 0.059 | 1.349 ± 0.067 | 1.426 ± 0.050 |
| | Electrons | LF | $2.32 \times 10^{-4} - 2.38 \times 10^{-3}$ | −0.825 | 0.690 ± 0.017 | 0.934 ± 0.025 | 0.850 ± 0.022 |
| | | IF | $2.38 \times 10^{-3} - 1.75 \times 10^{-2}$ | −0.730 | 0.774 ± 0.014 | 0.822 ± 0.008 | 0.805 ± 0.006 |
| | | HF | $1.75 \times 10^{-2} - 1.00 \times 10^{-1}$ | −0.100 | 0.847 ± 0.028 | 0.801 ± 0.018 | 0.817 ± 0.017 |

**Note.** $R_p(n_p, |\boldsymbol{B}|)$ is the Pearson correlation coefficient between $n_p$ and $|\boldsymbol{B}|$.

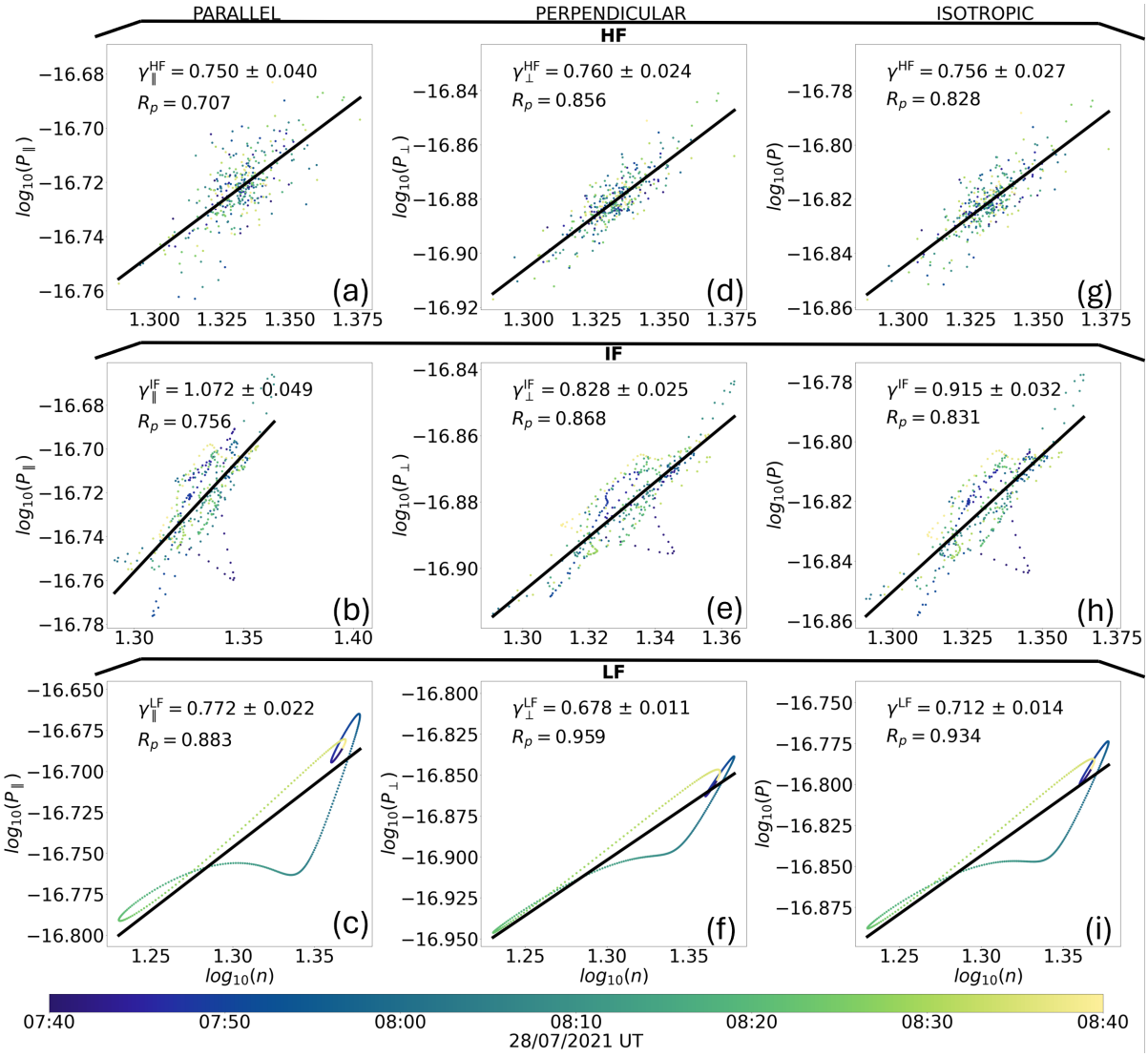


**Figure 8.** Polytropic index results of the decomposed signals for the electrons in CS1. Same format as Figure 7.

the proton plasma, furthered by the discrepancy between $\gamma_{1,p,\parallel}$ and the kinetic IA mode predictions. A closure with regards to the CGL polytropic indices is also observed in CS1, but the $\xi_{1,\parallel}$ and $\xi_{1,\perp}$ values differ from their adiabatic values of 3 and 2, respectively. This suggests that there is an exchange of energy between the particles and other reservoirs of heat in the surroundings. More work is required to understand the direction and magnitude of the energy exchange indicated by the $\xi_{1,\parallel}$ and $\xi_{1,\perp}$ values, which is beyond the scope of this paper. Thus, the fluid-like behavior of the protons is consistent with both MHD and CGL polytropic results.

Protons in CS2 exhibit behavior comparable to the IA mode. Specifically, $\gamma_{2,p,\parallel}$ approaches 3, the adiabatic index with $f = 1$, as predicted by the IA mode dispersion relationship (Equations (7) and (8)). Furthermore, the weaker correlation ($R_p < 0.5$) between $P_{p,\perp}$ and $n_p$, and the subisothermal value of $\gamma_{2,p,\perp}$ is contrary to the parallel polytropic behavior. Thus, the proton plasma exhibits anisotropic polytropic behavior, which is inconsistent with the MHD predictions. This is also evident by the fluctuations in the proton temperature anisotropy seen in Figure 2(f), which, considering that $\gamma_{2,p,\parallel} > \gamma_{2,p,\perp}$, means that the amplitude of the fluctuations in $T_{p,\parallel}$ is greater than the amplitude of the fluctuations in $T_{p,\perp}$. The CGL closure is poor, as evidenced in Figure 13, indicating the nonfluid nature of the compressive fluctuations in this event. Overall, as $\gamma_{2,p,\parallel}$ is near 3, the proton closure in CS2 is closest to that of an IA wave, in contrast to CS1.

Examining the temporal behavior of the data in Figures 6(b)–(c), two linear regression lines exist, separated in time. This can be evidence of a streamline crossing, despite the small variation in BI. However, this is not as clear when looking at the parallel case in Figure 6(a) and separating the interval into two events yields insignificant changes to the value of $\gamma_{2,p,\parallel}$, meaning that a proton behavior akin to the IA wave is observed whether the interval is clustered into two or kept intact. This temporal discrepancy of the event is not observed, however, when the signal is decomposed to shorter time scales, as seen in Figure 9.

In the scale-decomposed polytropic index results, we observe a shared scale dependence between the two events. The weak $n_p$, $|\boldsymbol{B}|$ anticorrelation in the HF band, present in both events, suggests that the slow mode is harder to measure at these scales. Thus, no clear conclusions regarding the nature of the slow mode at high frequencies can be made. At higher frequencies,

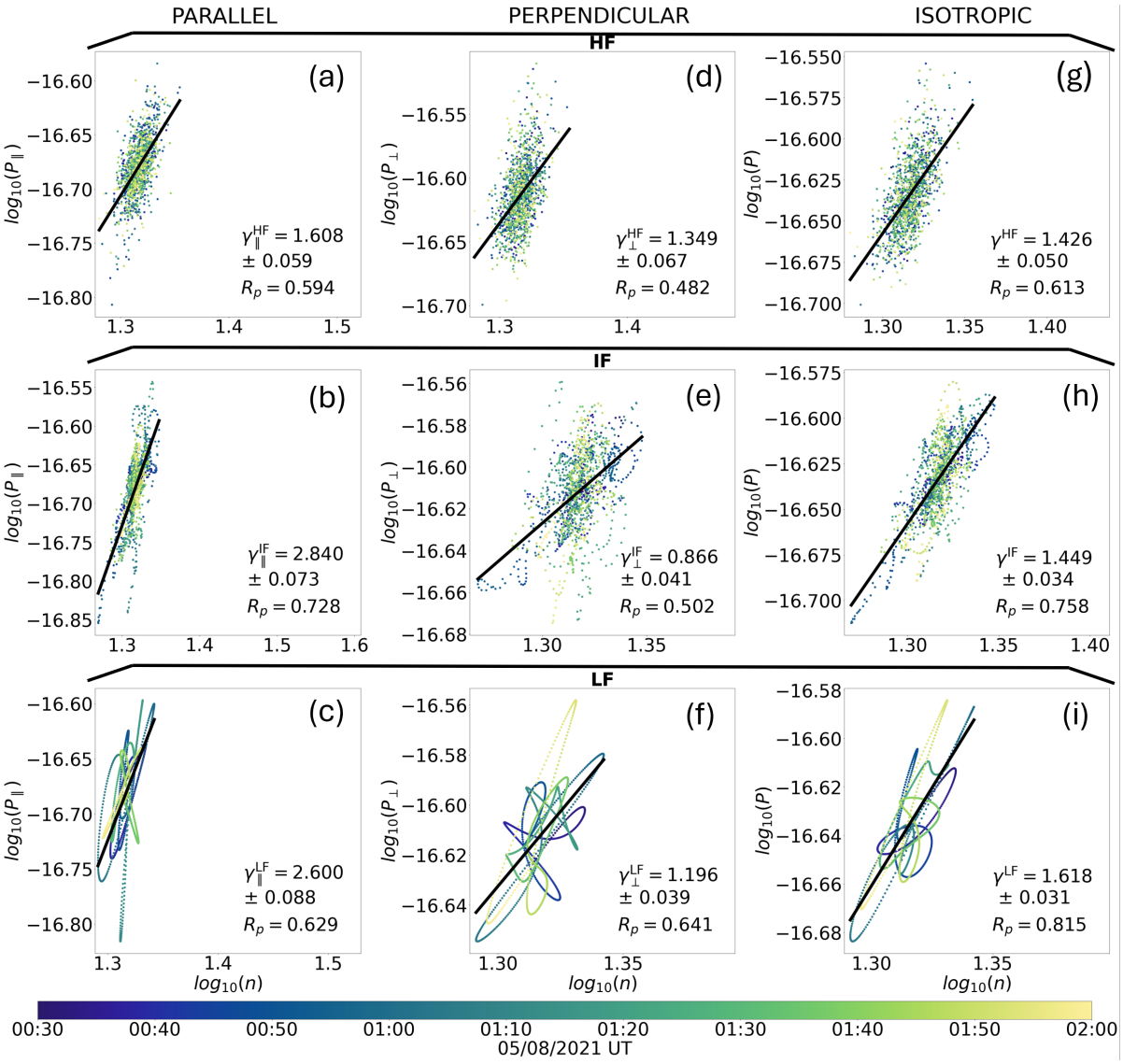


**Figure 9.** Polytropic index results of the decomposed signals for the protons in CS2. Same format as Figure 7.

the amplitude of the plasma fluctuations becomes small and could be comparable to the noise amplitude, preventing us from identifying possible correlations between the plasma parameters, leading to a smaller correlation coefficient.

The nature of the slow mode in the IF and LF bands is similar to the full signal, where protons in CS1 exhibit characteristics of the MHD slow mode, respecting the isotropic closure, while in CS2, a strong parallel closure with a polytropic index near 3 is evident, akin to the IA wave. The disparity between $\gamma_{p,\parallel}$ and $\gamma_{p,\perp}$ is larger in the IF band compared to the LF band in both events. This suggests that the plasma is more isotropic at larger scales and is an indication that the nature of the slow mode is also dependent on the length scale. At larger scales, the MHD slow mode is more persistent, while at smaller scales the disparity between $\gamma_{p,\parallel}$ and $\gamma_{p,\perp}$ increases as the kinetic properties of the compressive fluctuations become more evident, which is consistent with M. D. Tracy et al. (1993).

### 5.2. Electrons

The subisothermal behavior exhibited by the electrons in both events is inconsistent with both the MHD and the IA mode, which predict an isothermal electron plasma. This also differs from the electron large-scale radial trend of marginal superthermal ($\gamma > 1$) behavior (J. B. Abraham et al. 2022). This deviation from the large-scale radial electron trends can be attributed to the fact that we only investigate a localized streamline which may exhibit significantly varied behavior from the average solar wind conditions.

However, the mechanisms behind the subisothermal electron behavior remain unclear. We investigated the possibility of electrons becoming trapped by the fluctuating magnetic field by plotting the pitch angle distribution function of energetic electrons, similarly to W. Jiang et al. (2022), but the $\boldsymbol{B}$ field fluctuations are not strong enough to trap a considerable fraction of the electron population. Additionally, we note that the proton and electron temperatures are anticorrelated in both events. A non-Maxwellian electron distribution could explain the deviation from the MHD and IA predictions, but the specifics behind the subisothermal electron behavior remain an open question. A statistical study containing a larger number of intervals and delving deeper into the thermal energy budget

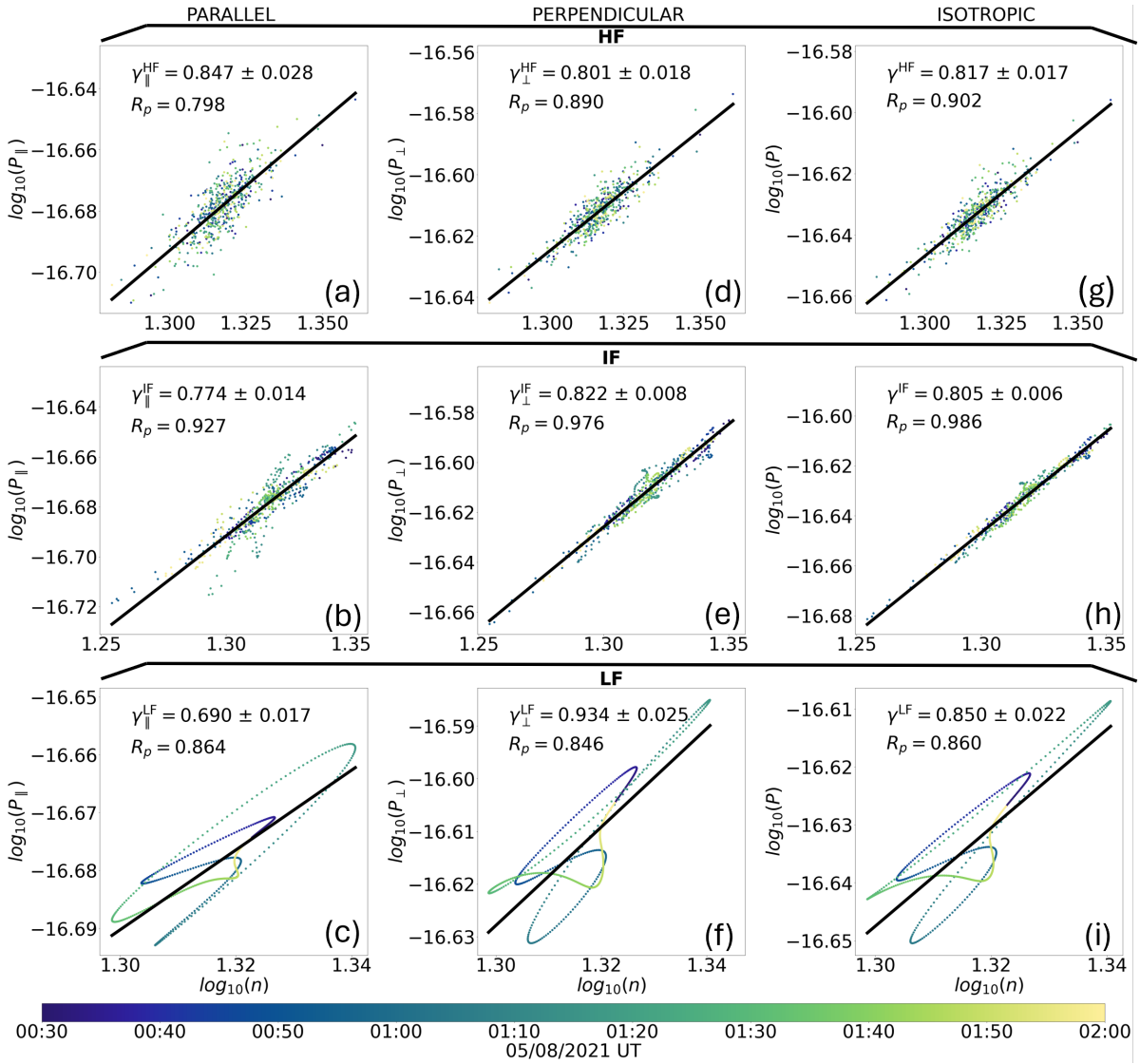


**Figure 10.** Polytropic index results of the decomposed signals for the electrons in CS2. Same format as Figure 7.

of electrons, beyond the simple polytropic model, would be required to better answer this question.

### 5.3. Comparison of Both Intervals

We have seen that the proton plasma in CS1 exhibits properties consistent with that of a fluid characterized by the MHD slow mode, while in CS2, protons exhibit behavior closer to the IA mode. To gain further insight into the mechanisms and nature behind the differences between the two events, we investigate additional properties of the solar wind plasma. The magnetic field and density power spectrums were determined for both events, with no evident discrepancies between the two.

To compare the Coulomb collisionality of the plasma between the two events, we calculate the Spitzer–Härm proton–proton collision frequency, $\nu^{SH}$ (L. Spitzer 1962). The collision frequency of CS1 is found to be $\nu_2^{SH} = 2.66 \times 10^{-6}\,s^{-1}$, approximately double that of CS2, $\nu_2^{SH} = 1.31 \times 10^{-6}\,s^{-1}$. The Spitzer–Härm mean free path is not an accurate measure of the effective collisionality of the proton plasma because it is orders of magnitude larger than the effective proton mean free path (J. T. Coburn et al. 2022). However, the fact that $\nu_1^{SH} \approx 2\nu_2^{SH}$ suggests that the plasma in CS1 experiences more Coulomb collisions than in CS2.

To further assess the differences in the Coulomb collisionality of the plasma between the two events, we determine the velocity boundary, $V_D$, (in the plasma frame) where the plasma becomes collisional (collision number $> 1$), as defined by E. Marsch & H. Goldstein (1983). We then determine the ratio between $V_D$ and $V_{th}$. The ratio is greater for CS1, $V_{D,1}/V_{th,1} = 1.05$, compared to that of CS2, $V_{D,2}/V_{th,2} = 0.74$. This indicates that a larger fraction of the proton population in CS1 is affected by Coulomb collisions compared to CS2, which is consistent with the Spitzer–Härm collision frequency estimates of the two events. Thus, the level of Coulomb collisions differs in both intervals, but the difference is not massive. Nevertheless, Coulomb collisions could be a candidate for fluidization, which could explain the different proton polytropic behavior between the two events.

Even collisionless processes have the ability to fluidize the plasma behavior. For instance, antiphase-mixing due to the stochastic counterpart of the plasma echo effect suppresses higher-order moments of the plasma VDF, and thus creates an

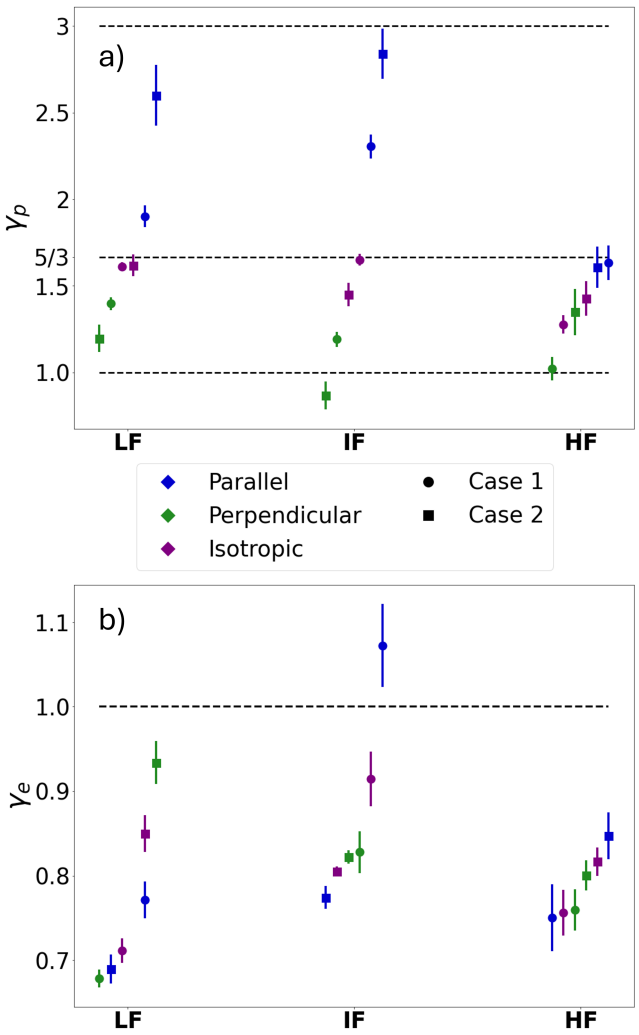


**Figure 11.** Multiscale $\gamma$ results for (a) protons and (b) electrons. The • and ■ markers show CS1 and CS2 results, respectively. The blue points show the parallel, the green the perpendicular, and the purple the isotropic $\gamma$ results. The $2\sigma$ error is shown for the protons to enhance visibility.

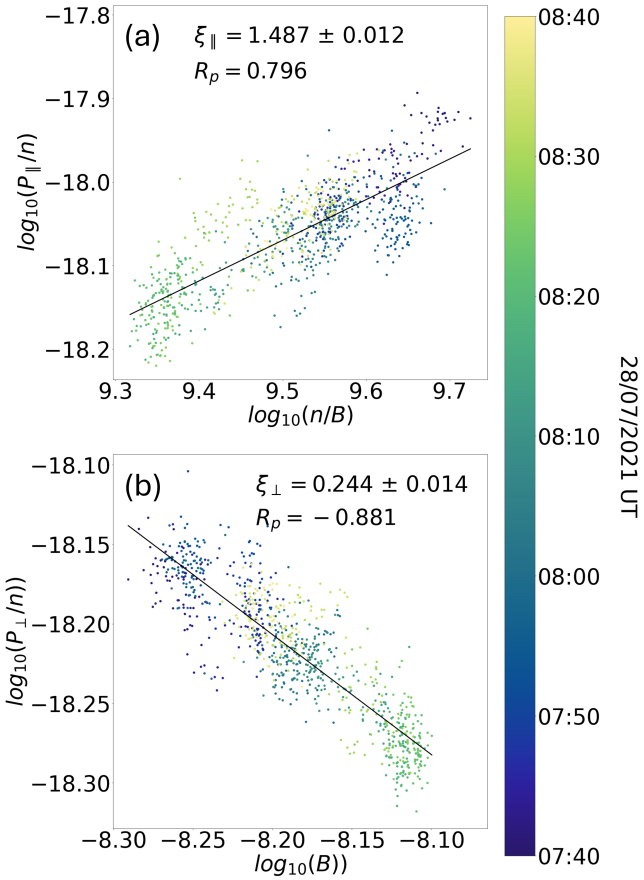


**Figure 12.** CGL proton polytropic index results for CS1. $R_p$ is the Pearson correlation coefficient. Panel (a) shows the results for $\xi_\parallel$ and panel (b) for $\xi_\perp$. The color of the data points represents the time instance of the corresponding measurement in the interval.

effective lower-moment closure (A. A. Schekochihin et al. 2016). Moreover, wave–particle interactions can act effectively like collisions even under collisionless conditions and thus also fluidize the plasma behavior (G. G. Howes et al. 2018). Quantifying the effective collisionality of these would be worthwhile for a future study as an important aspect of collisionless thermodynamics, since it can provide more insight into the mechanisms behind the differing nature of the two events.

## 6. Conclusions

We report two case studies of compressive fluctuations in the solar wind observed by Solar Orbiter. We employ standard methods to characterize the potential polytropic closure between the pressure and density of protons and electrons in these compressive fluctuations. We discuss our results with reference to the predictions of the MHD and CGL slow modes and the IA wave. Electrons show similar polytropic properties in both cases, exhibiting subisothermal behavior with $\gamma_e \approx 0.7$, and no significant variance between $\gamma_{e,\parallel}$ and $\gamma_{e,\perp}$. This value is lower than the MHD slow mode and IA wave predictions of $\gamma_e \approx 1$.

The proton polytropic behavior is significantly different between the two events. In the first event, we report an isotropic polytropic closure with $\gamma_{1,p} \approx 1.7$, matching the MHD slow-mode predictions, with small variation in the parallel and perpendicular directions where $\gamma_{1,p,\parallel} \approx 1.9$ and $\gamma_{1,p,\perp} \approx 1.6$. The second case study exhibits anisotropic polytropic behavior, where $\gamma_{2,p,\parallel} \approx 2.8$, which is comparable to the IA wave prediction of $\gamma_{p,\parallel} = 3$, while the polytropic closure is significantly weaker in the perpendicular direction, as indicated by a lower Pearson correlation coefficient. A CGL polytropic closure is evident in case 1, but $\xi_{1,\parallel}$ and $\xi_{1,\perp}$ are not comparable to the adiabatic values of 3 and 2, and the existence of a CGL closure is less evident in CS2.

Furthermore, we applied three frequency filters to the density and pressure signals to investigate the frequency dependence on the polytropic results. In the highest frequency band, we do not clearly observe the slow mode because the anticorrelation between $n$ and $|\boldsymbol{B}|$ is significantly weaker. In the intermediate and lowest frequency bands, the proton polytropic behavior between the two events is analogous to the full signal, where case 1 is comparable to the MHD slow mode while case 2 is more akin to the IA mode. However, we also observe a subtle frequency dependence on the results. The difference between $\gamma_{p,\parallel}$ and $\gamma_{p,\perp}$ is higher in the IF band,

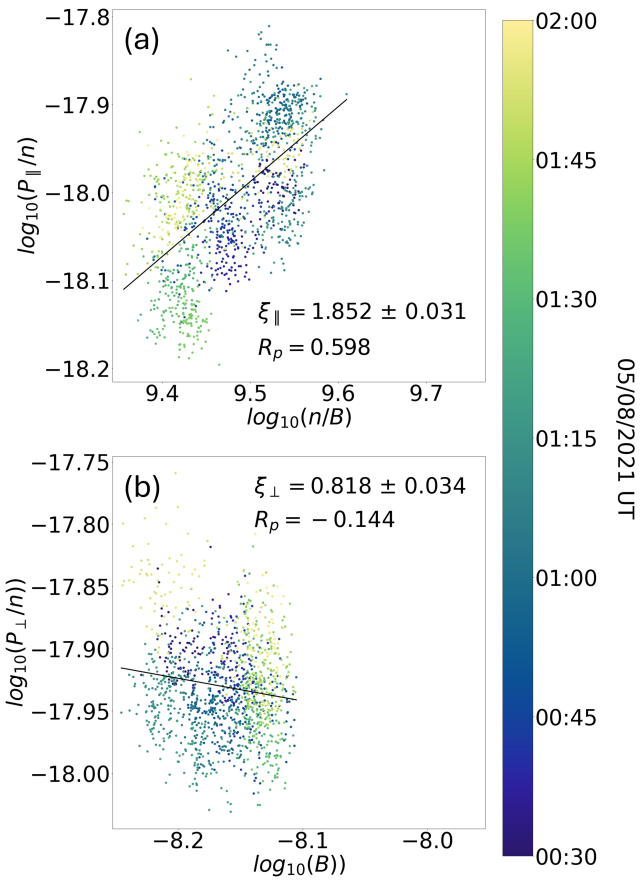


**Figure 13.** CGL proton polytropic index results for CS2. Same format as Figure 12.

which may suggest that kinetic effects introducing anisotropic behavior become more prominent at shorter time scales.

The mechanisms behind the differing natures of the slow mode between the two cases remain unclear. We find that the Spitzer–Härm proton–proton collision frequency, while not representative of the effective collisionality experienced by the solar wind, is approximately double in case 1 compared to case 2. Additionally, using a method identical to E. Marsch & H. Goldstein (1983), we find that a larger fraction of the proton population is dominated by collisions in case 1 when compared to case 2, which may explain the different nature of the compressive fluctuations in the two events. A statistical study comprising a larger data set of compressive fluctuations would provide further insight into the reasons behind the varying emergence and behavior of the slow mode in the solar wind.

## Acknowledgments

C.I. acknowledges STFC's support through the PhD degree (ST/X508858/1). L.F. is supported by the Royal Society University Research Fellowship No. URF/R1/231710 and was supported by the Science and Technology Facilities council (STFC) grant ST/W001071/1. Solar Orbiter is a space mission of international collaboration between ESA and NASA, operated by ESA. Solar Orbiter Solar Wind Analyser (SWA) data are derived from scientific sensors which have been designed and created, and are operated under funding provided in numerous contracts from the UK Space Agency (UKSA), the UK Science and Technology Facilities Council (STFC), the Agenzia Spaziale Italiana (ASI), the Centre National d'Etudes Spatiales (CNES, France), the Centre National de la Recherche Scientifique (CNRS, France), the Czech contribution to the ESA PRODEX program, and NASA. The Solar Orbiter SWA work at UCL/MSSL was funded under STFC grants ST/W001004/1 and ST/X/002152/1. This work was supported by the Czech Science Foundation (GAˇCR), project No. 23-07334S. The authors further acknowledge collaboration with the SWA-EAS and RPW instrument teams when discussing any technical, calibration, or data product related issues.

## ORCID iDs

C. Ioannou https://orcid.org/0000-0003-4398-9931
G. Nicolaou https://orcid.org/0000-0003-3623-4928
C. J. Owen https://orcid.org/0000-0002-5982-4667
D. Verscharen https://orcid.org/0000-0002-0497-1096
J. T. Coburn https://orcid.org/0000-0002-2576-0992
L. Franci https://orcid.org/0000-0002-7419-0527

## References

Abraham, J. B., Verscharen, D., Wicks, R. T., et al. 2022, ApJ, 941, 145
Abraham-Shrauner, B. 1973, PlPh, 15, 375
Bavassano, B., & Bruno, R. 1989, JGRA, 94, 11977
Bavassano, B., Bruno, R., & Rosenbauer, H. 1996, AnGeo, 14, 510
Burlaga, L. F., & Ogilvie, K. W. 1970, SoPh, 15, 61
Chandrasekhar, S. 1957, An Introduction to the Study of Stellar Structure (New York: Dover Publications)
Chen, C. H. K. 2016, JPlPh, 82, 535820602
Chew, G. F., Goldberger, M. L., Low, F. E., & Chandrasekhar, S. 1956, RSPSA: Mathematical and Physical Sciences, 236, 112
Cicone, A., & Pellegrino, E. 2022, ITSP, 70, 1521
Coburn, J. T., Chen, C. H. K., & Squire, J. 2022, JPlPh, 88, 175880502
Gary, S. P. 1993, Theory of Space Plasma Microinstabilities, Cambridge Atmospheric and Space Science Series (Cambridge: Cambridge Univ. Press)
Grinsted, A., Moore, J. C., & Jevrejeva, S. 2004, NPGeo, 11, 561
Hau, L. N., & Sonnerup, B. U. O. 1993, GeoRL, 20, 1763
Horbury, T. S., O'Brien, H., Blazquez, I. C., et al. 2020, A&A, 642, A9
Howes, G. G., Bale, S. D., Klein, K. G., et al. 2012, ApJL, 753, L19
Howes, G. G., Cowley, S. C., Dorland, W., et al. 2006, ApJ, 651, 590
Howes, G. G., McCubbin, A. J., & Klein, K. G. 2018, JPlPh, 84, 905840105
Huang, N. E., Shen, Z., Long, S. R., et al. 1998, RSPSA: Mathematical, Physical and Engineering Sciences, 454, 903
Hunana, P., Tenerani, A., Zank, G. P., et al. 2019, JPlPh, 85, 205850602
Jiang, W., Verscharen, D., Li, H., Wang, C., & Klein, K. G. 2022, ApJ, 935, 169
Kartalev, M., Dryer, M., Grigorov, K., & Stoimenova, E. 2006, JGRA, 111, A10107
Katsavrias, C., Nicolaou, G., Matteo, S. D., et al. 2024, A&A, 686, L10
Kellogg, P. J., & Horbury, T. S. 2005, AnGeo, 23, 3765
Klein, K. G., Howes, G. G., TenBarge, J. M., et al. 2012, ApJ, 755, 159
Kunz, M. W., Squire, J., Schekochihin, A. A., & Quataert, E. 2020, JPlPh, 86, 905860603
Livadiotis, G., & Nicolaou, G. 2021, ApJ, 909, 127
Maksimovic, M., Bale, S. D., Chust, T., et al. 2020, A&A, 642, A12
Marsch, E., & Goldstein, H. 1983, JGRA, 88, 9933
Marsch, E., & Richter, A. K. 1984, JGRA, 89, 6599
Meyrand, R., Kanekar, A., Dorland, W., & Schekochihin, A. A. 2019, PNAS, 116, 1185
Müller, D., Cyr, O. C. S., Zouganelis, I., et al. 2020, A&A, 642, A1
Narita, Y., & Marsch, E. 2015, ApJ, 805, 24
Newbury, J. A., Russell, C. T., & Lindsay, G. M. 1997, GeoRL, 24, 1431
Nicolaou, G., & Livadiotis, G. 2017, ApJ, 838, 7
Nicolaou, G., & Livadiotis, G. 2019, ApJ, 884, 52
Nicolaou, G., Livadiotis, G., & Desai, M. I. 2021a, ApSci, 11, 4643
Nicolaou, G., Livadiotis, G., & McComas, D. J. 2023, ApJ, 948, 22
Nicolaou, G., Livadiotis, G., & Moussas, X. 2014, SoPh, 289, 1371
Nicolaou, G., Livadiotis, G., Wicks, R. T., Verscharen, D., & Maruca, B. A. 2020, ApJ, 901, 26

Nicolaou, G., Wicks, R. T., Owen, C. J., et al. 2021b, A&A, 656, A10
Owen, C. J., Bruno, R., Livi, S., et al. 2020, A&A, 642, A16
Papini, E., Cicone, A., Piersanti, M., et al. 2020, JPlPh, 86, 871860501
Schekochihin, A. A., Parker, J. T., Highcock, E. G., et al. 2016, JPlPh, 82, 905820212
Spitzer, L. 1962, Physics of Fully Ionized Gases (New York: Interscience)
Šafránková, J., Němeček, Z., Němec, F., et al. 2019, ApJ, 870, 40
Štverák, S., Herčík, D., Nicolaou, G., et al. 2025, A&A, 693, A185
Torrence, C., & Compo, G. P. 1998, BAMS, 79, 61
Totten, T. L., Freeman, J. W., & Arya, S. 1995, JGR, 100, 13
Tracy, M. D., Williams, E. A., Estabrook, K. G., De Groot, J. S., & Cameron, S. M. 1993, PhFlB, 5, 1430
Tu, C. Y., & Marsch, E. 1995, SSRv, 73, 1
Verscharen, D., Chandran, B. D. G., Klein, K. G., & Quataert, E. 2016, ApJ, 831, 128
Verscharen, D., Chen, C. H. K., & Wicks, R. T. 2017, ApJ, 840, 106
Yao, S., He, J.-S., Marsch, E., et al. 2011, ApJ, 728, 146
Yao, S., He, J.-S., Tu, C.-Y., Wang, L.-H., & Marsch, E. 2013, ApJ, 774, 59
Zhu, X., Verscharen, D., He, J., Maruca, B. A., & Owen, C. J. 2023, ApJ, 956, 66